

## Electronic noise of a single skyrmion

Kang Wang<sup>✉</sup>,\* Yiou Zhang<sup>✉</sup>, Vineetha Bheemarasetty<sup>✉</sup>, See-Chen Ying<sup>✉</sup>, and Gang Xiao<sup>✉</sup><sup>†</sup>

Department of Physics, Brown University, Providence, Rhode Island 02912, USA



(Received 20 June 2023; revised 14 August 2023; accepted 12 September 2023; published 22 September 2023)

To enable the practical use of skyrmion-based devices, it is essential to achieve a balance between energy efficiency and thermal stability while also ensuring reliable electrical detection against noise. Understanding how a skyrmion interacts with material disorder and external perturbations is thus essential. Here, we investigate the electronic noise of a single skyrmion under the influence of thermal fluctuations and spin currents in a magnetic thin film. We detect the thermally induced noise with a  $1/f^\gamma$  signature in the strong pinning regime but a random telegraph noise in the intermediate pinning regime. Both the thermally dominated and current-induced telegraphlike signals are detected in the weak pinning regime. Our results provide a comprehensive electronic noise picture of a single skyrmion, demonstrating the potential of noise fluctuation as a valuable tool for characterizing the pinning condition of a skyrmion. These insights could also aid in the development of low-noise and reliable skyrmion-based devices.

DOI: [10.1103/PhysRevB.108.094431](https://doi.org/10.1103/PhysRevB.108.094431)

### I. INTRODUCTION

Noise fluctuation is conveniently analyzed through its power spectrum:

$$S(\omega) = \left| \int_{t_1}^{t_2} x(t) \exp(-i2\pi\omega t) dt \right|^2, \quad (1)$$

where  $x(t)$  is the time-domain signal. The power spectrum possesses various signatures which may provide information about the nature of the dynamics. For example, a broadband  $1/f^\gamma$  ( $f = 2\pi\omega$ ) noise may be detected. While the noise is white when  $\gamma = 0$ , the  $1/f^2$  signature ( $\gamma = 2$ ) corresponds to Brownian noise and can be produced by the trajectories of a Brownian walk. According to Van Der Ziel's [1] picture [2,3], the  $1/f^\gamma$  signature may arise from a collection of nonidentical random telegraph noise (RTN) oscillators with the form:

$$S_x(f) = \frac{\Delta x^2}{2f_0} \frac{1}{1 + (\pi f/f_0)^2}, \quad (2)$$

where  $f_0$  is the average fluctuation rate, and  $\Delta x$  is the difference of the quantity  $x$  between the two states. In addition to broadband noise, there may also be a narrow band noise in the detection which produces peaks at characteristic frequencies that correspond to the length scales of the system [4–8].

Noise fluctuation has proven to be a useful method for characterizing condensed matter states such as superconducting vortices [4,5,9–12], quantum fluctuations [13–18], and charge density waves [19–24]. It could be equally useful for characterizing skyrmions. Magnetic skyrmions with a fixed chirality have been observed in noncentrosymmetric bulk magnets [25–27] and magnetic multilayers [28–32], where

the antisymmetric Dzyaloshinskii-Moriya interaction (DMI) [33,34] exists and favors one sense of rotation of the magnetization over the other. Magnetic skyrmions can serve as effective agents for next-generation beyond-CMOS data storage [35–38], logic [39–41], probabilistic computing [42–45], and neuromorphic computing [46] devices owing to their nonvolatility, stability, and efficient controllability. For device applications, it is necessary to manipulate a single skyrmion via spin currents [35,36,39,40,45,46], magnetic fields, or microscopic thermal fluctuations [42–45]. This must be achieved in an efficient manner while recognizing that there is a tradeoff between energy efficiency and thermal stability. Furthermore, one must be able to transduce a single skyrmion into detectable electrical signals against noise. These requirements demand an understanding of how a skyrmion interacts with material disorder and external perturbations. Alternatively, one may take advantage of the noise in devices such as a skyrmion true random number generator [45]. A comprehensive study of the noise properties of a skyrmion is therefore crucial and may provide fundamental guidance on how to fabricate devices that demand low-noise performance and reliable electrical detection as well as those that utilize the noise fluctuation of a skyrmion.

The noise characterization of skyrmions has been limited to particle-based models [6,47] and only recently has been studied experimentally for the motion of a skyrmion lattice in a bulk magnet with a B20 crystal structure [7,8]. It was found that the collective transport of a skyrmion lattice produces a narrow band noise with the washboard frequency corresponding to the time required for a skyrmion particle to move one period. The electronic noise of a single skyrmion, however, remains elusive. The formation of a skyrmion configuration is a result of the delicate balance between competing energies. In materials with disorder, the size and shape of a skyrmion can vary spatially [48]. The shape of the encircling domain wall around the skyrmion core is governed by the competition

\*kwang@hmfl.ac.cn

<sup>†</sup>gang\_xiao@brown.edu

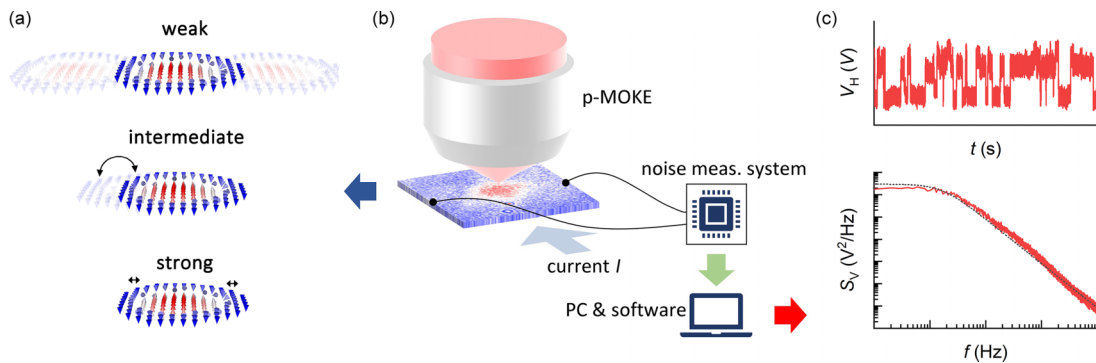


FIG. 1. Scheme of the experimental setup for studying noise of a skyrmion. (a) A schematic depiction of pinning effects on the noise dynamics of a skyrmion. In the strong pinning regime, the skyrmion is strongly pinned, while multiple internal domain-wall hopping oscillations (double-headed arrows) may exist. In the intermediate pinning regime, one case is presented where one part of a skyrmion is more strongly pinned while the other part, under thermal effects, fluctuates in time between two weaker pinning sites, leading to a random telegraph noise signature. In the weak pinning regime, the skyrmions hop between pinning sites more easily, and both temperature and current can strongly affect the skyrmion dynamics. (b) Schematic of the experimental setup. Electronic noise of a skyrmion is studied by an electronic noise measurement system with the help of direct imaging using a polar magneto-optic Kerr effect (p-MOKE) microscope. (c) An example of the Hall voltage  $V_H(t)$  and its power spectrum  $S_V(f)$  obtained by the noise measurement system.

between skyrmion surface tension energy [49,50] and local pinning energy [48,51]. Additionally, external perturbations can induce spin torques on the magnetization, causing local fluctuations that generate noise in the skyrmion.

In this paper, we perform a systematic study of the electronic noise produced by a single skyrmion in response to thermal fluctuations and spin currents over a wide range of pinning conditions. We detect and analyze distinct noise signatures from the thermally dominated and current-induced dynamics of a skyrmion. This study helps us understand how a skyrmion interacts with material disorder and perturbations, which is also key to understanding the noise dynamics of other structures in physics that share similar behaviors.

## II. MAGNETIC THIN FILMS AND MAGNETIC STRUCTURES

For this paper, we fabricate perpendicularly magnetized multilayers of substrate/Ta/Co<sub>40</sub>Fe<sub>40</sub>B<sub>20</sub>(0.95 nm)/MgO(1.6 nm)/TaO<sub>x</sub> on thermally oxidized silicon wafers (Supplemental Material Note I [52]). The magnetic configuration in this system is determined by the competition between multiple energy terms, including the perpendicular magnetic anisotropy [53–56], exchange interaction, interfacial DMI [33,34], and Zeeman energy, and can be tuned by an applied perpendicular magnetic field  $H_z$  (Supplemental Material Note III and Fig. S3 [52,57,58]). The interfacial DMI leads to chiral magnetic domain walls and stabilizes skyrmions in this system at room temperature and in a suitable field range (Supplemental Material Notes III and IV [52]).

We implement moderate pinning strengths by regulating the DC power ( $P_{Ta}$ ) for deposition of the Ta layer (Supplemental Material Note V [52]). We identify the three growth scenarios with  $P_{Ta} = 3, 4$ , and 5 Watt as corresponding to the strong, intermediate, and weakly pinned samples, respectively (Supplemental Material Note V and Movies 1–3 [52]). Distinct pinning conditions may result from the effects of  $P_{Ta}$  on thin-film structures and the variation in material parameters (Supplemental Material Note V [52]), which also contains

Refs. [51,59–80]). The competition between the pinning energy, thermal energy, and the current determines the noise dynamics of a skyrmion, as shown in Fig. 1(a) and discussed in more detail below.

To study the electronic noise of a skyrmion, we nucleate a single skyrmion in a  $20 \times 20 \mu\text{m}^2$  Hall cross and measure the magnetically induced Hall signal fluctuations (Supplemental Material Note II [52,81–84] and Fig. 1(b)). In this case, the  $x$  in Eqs. (1) and (2) is defined as the Hall voltage  $V_H = R_H I$ , where  $R_H$  is the Hall resistance. Notably,  $R_H$  is dominated by the anomalous Hall resistance that is proportional to the perpendicular magnetization, while the conventional Hall resistance proportional to  $H_z$  can be neglected in comparison [85]. We measure the noise under an applied current  $I$  and a perpendicular magnetic field  $H_z$ . The electric current is converted into a spin current through the spin Hall solid Ta, which exerts spin-orbit torques on the skyrmion [86–88]. This study provides us with both amplitude and frequency details of the noise of a skyrmion in response to the external perturbations.

## III. ELECTRONIC NOISE OF A SKYRMION IN DIFFERENT PINNING REGIMES

We summarize in Fig. 2 the electronic noise results of a single skyrmion in the strong, intermediate, and weak pinning regimes. All results are measured in the temperature range from 298.9 to 319.5 K and in the current range from 0.01 to 1.0 mA. As described in more detail below, we detect a thermally induced noise with a  $1/f^\gamma$  signature in the strong pinning regime (Fig. 3) but a RTN in the intermediate pinning regime (Fig. 4). Both the thermally dominated and current-induced telegraphlike signals are detected in the weak pinning regime (Fig. 5).

Figure 2(b) summarizes the amplitude details of the noise of a skyrmion for each pinning region. Instead of presenting noise  $S_R$ , we present a normalized Hall resistance noise  $\Delta S_R^{\text{Skyr}} / (\Delta R_{xy}^{\text{Skyr}})^2$ , where  $\Delta R_{xy}^{\text{Skyr}}$  and  $\Delta S_R^{\text{Skyr}}$  are average contributions of each skyrmion to the anomalous Hall resistance and Hall resistance noise, respectively, as discussed below.

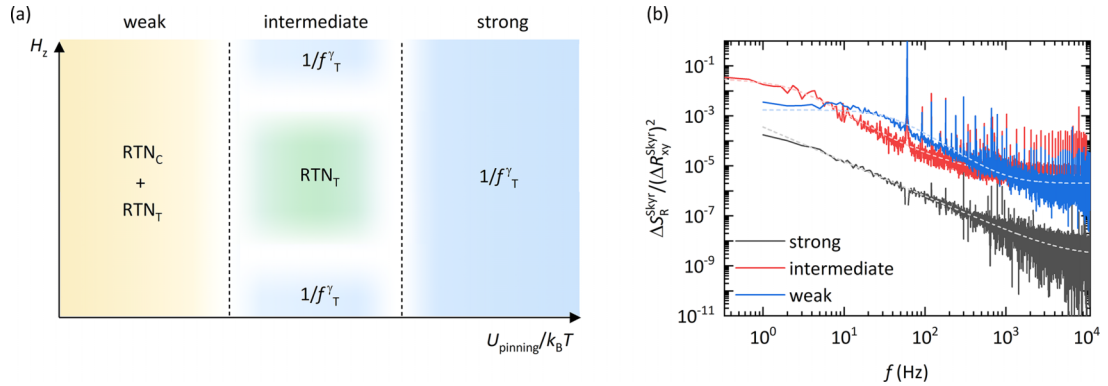


FIG. 2. (a) Summary of electronic noise of a skyrmion  $n$  in different pinning regimes. The subscripts T and C represent the noise of thermally dominated or current-induced dynamics, respectively. We detect a thermally induced noise with a  $1/f^\gamma$  signature in the strong pinning regime but a random telegraph noise (RTN) in the intermediate pinning regime. Both the thermally induced and current-induced telegraphlike signals are detected in the weak pinning regime. (b) Normalized Hall resistance noise  $\Delta S_R^{\text{Skyr}} / (\Delta R_{xy}^{\text{Skyr}})^2$  of a skyrmion in different pinning regimes.  $\Delta R_{xy}^{\text{Skyr}}$  and  $\Delta S_R^{\text{Skyr}}$  represent average contributions of each skyrmion to the anomalous Hall resistance and Hall resistance noise, respectively. In the intermediate and weak pinning regimes, we make the approximation that  $\Delta S_R^{\text{Skyr}} \approx S_R$  for  $N_{\text{Skyr}} = 1$ . This is justified as the  $S_R$  for  $N_{\text{Skyr}} = 1$  significantly exceeds the background noise level, which can be disregarded in our calculations.

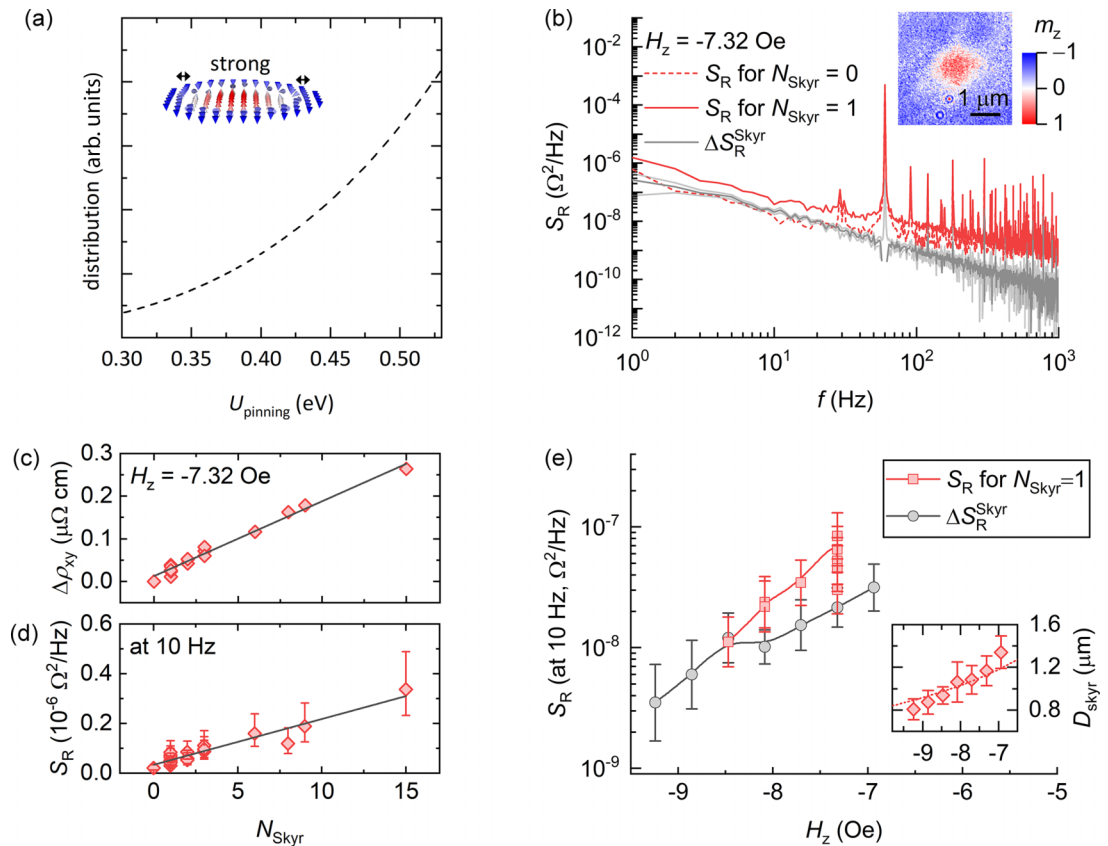


FIG. 3.  $1/f^\gamma$  noise of a skyrmion in the strong pinning regime. (a) A plot illustrating distribution of the  $U_{\text{pinning}}$  that contribute to the  $1/f^\gamma$  noise of a skyrmion. The result is obtained by fitting the gray curve in (b), which exhibits a  $1/f^\gamma$  signature with  $\gamma = 1.36$ . The inset provides a schematic depiction of the noise dynamics of a skyrmion under strong pinning, where the skyrmion is strongly immobilized while potentially undergoing multiple internal domain-wall hopping oscillations (double-headed arrows). (b) Red dashed line:  $S_R$  spectra with the  $1/f^\gamma$  noise signature for  $N_{\text{Skyr}} = 0$  at  $H_z = -7.32$  Oe. Red solid line:  $S_R$  spectra with the  $1/f^\gamma$  noise signature for  $N_{\text{Skyr}} = 1$  at  $H_z = -7.32$  Oe. Gray line: an average contribution of each skyrmion to the noise  $\Delta S_R^{\text{Skyr}}$ , where the background noise is subtracted. The inset shows a p-MOKE image of the skyrmion for noise measurements. (c) The relative Hall resistivity  $\Delta \rho_{xy}$  as a function of  $N_{\text{Skyr}}$ . (d)  $S_R$  at 10 Hz as a function of  $N_{\text{Skyr}}$ . The dotted line is a linear fit to  $S_R = S_{R,0} + \Delta S_R^{\text{Skyr}} N_{\text{Skyr}}$ . (e)  $S_R$  for  $N_{\text{Skyr}} = 1$ ,  $\Delta S_R^{\text{Skyr}}$  and the skyrmion diameter  $D_{\text{Skyr}}$  as a function of  $H_z$ . Dotted line in the inset represents the fit to the experimental data using a theoretical model [89] (Supplemental Material Note II [45,52,88,89]).

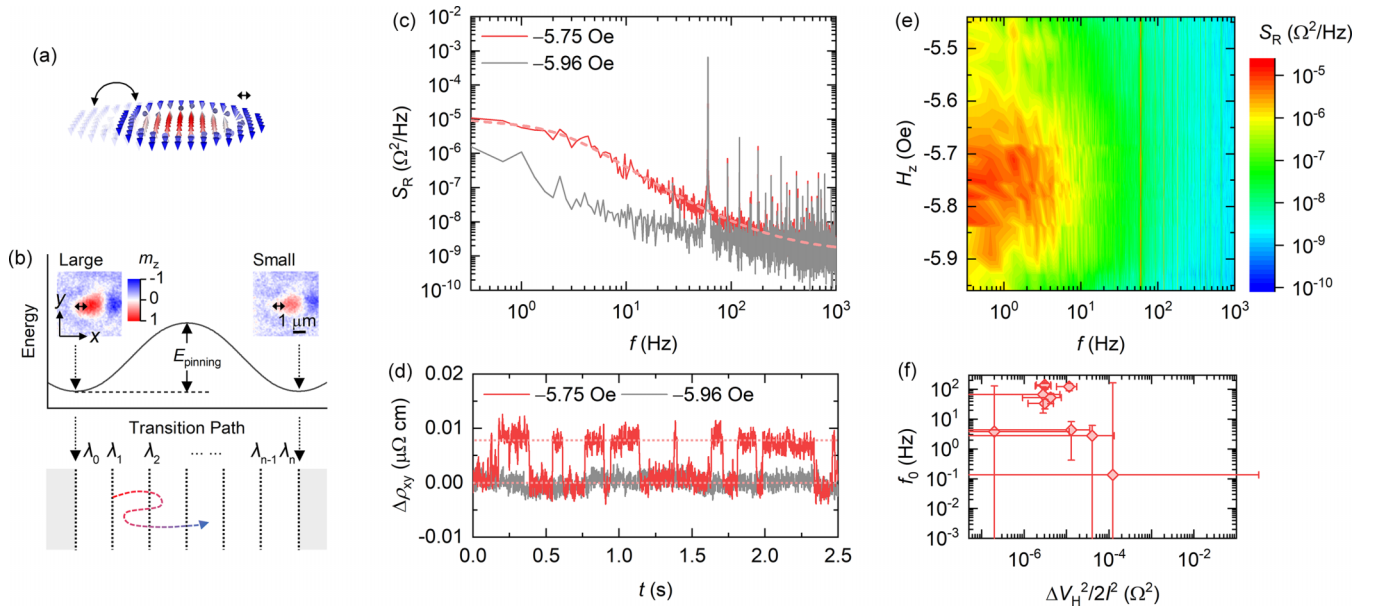


FIG. 4. Random telegraph noise (RTN) of a skyrmion in the intermediate pinning regime. (a) Schematic depiction of skyrmion dynamics in the intermediate pinning regime. The case presented here involves one part of a skyrmion being more strongly pinned while the other part, under thermal effects, fluctuates in time between two weaker pinning sites leading to a RTN signature. (b) Energy path for the two-state transition. The small- and large-skyrmion states occur at local minima in the energy landscape separated by an energy barrier. The transition between the two states involves passing through a series of interfaces,  $\{\lambda_L = \lambda_0, \lambda_1, \dots, \lambda_{n-1}, \lambda_n = \lambda_S\}$ , defined as isosurfaces of a monotonically varying order parameter  $\zeta$ , such as the perpendicular magnetization  $m_z$ . Due to the presence of thermal energy, recrossings between neighboring interfaces are inevitable, as illustrated by the dashed arrow in the schematic. (c) Hall resistance noise spectra  $S_R$  of a skyrmion in the intermediate pinning regime. The spectra are measured at  $H_z = -5.75$  Oe (red) and  $-5.96$  Oe (gray), where the skyrmion fluctuates in time between the two states or remains in a deterministic small-skyrmion state, respectively. The dashed line is a fit to the RTN plus a  $1/f^\gamma$  noise. (d) Relative Hall resistivity  $\Delta\rho_{xy}$  variations in time of a skyrmion at  $H_z = -5.75$  Oe (red) and  $-5.96$  Oe (gray). (e) Map of Hall resistance noise spectra  $S_R$  at different fields. A transition of the RTN into the  $1/f^\gamma$  noise is observed by increasing or decreasing the field to the deterministic small- and large-skyrmion states, respectively. (f) The fluctuation rate  $f_0$  as a function of the amplitude  $\Delta V_H^2/2I^2$  of the RTN of isolated skyrmions in the intermediate pinning regime. All results are measured at 307.1 K and with a current  $I = -0.2$  mA. This current corresponds to the current density of  $-2.4 \times 10^9$  A/m<sup>2</sup> flowing in the Ta buffer layer. The red curve in (d) is reproduced from Ref. [45].

The normalized noise accounts for the variations in the Hall resistance of a single skyrmion across different samples and therefore allows us to compare different samples.

#### A. $1/f^\gamma$ noise of a skyrmion in the strong pinning regime

In the strong pinning regime, skyrmions move negligibly owing to the lower thermal energy relative to the pinning energy  $U_{\text{pinning}}$ . Still, the internal domain-wall hopping exists and may contribute to the  $1/f^\gamma$  noise signature (Fig. 3(b), also see Supplemental Material Note VI and Figs. S7 and S8 [52], Note VI also contains Refs. [90–92]). The speculation of internal domain-wall hopping oscillations contributing to the  $1/f^\gamma$  noise of a skyrmion finds validation through micromagnetic simulations as depicted in Supplemental Material Note VII and Fig. S9 [52] (Note VII also contains Ref. [93]). The pinning energy  $U_{\text{pinning}}$  governs the domain-wall hopping through the Arrhenius law  $f_0 = f_{00}\exp(-U_{\text{pinning}}/k_B T)$ , where  $f_{00}$  is the attempt frequency. The  $U_{\text{pinning}}$  distribution therefore affects the distribution of the internal domain-wall hopping oscillators as well as the noise signature from this collection of nonidentical oscillators. Conversely, the distribution of  $U_{\text{pinning}}$  can be inferred through an examination of

the noise spectrum. When the distribution is uniform,  $\gamma = 1$ . A fitting of the  $1/f^\gamma$  noise with  $\gamma = 1.36$  [gray curve in Fig. 3(b)] uncovers the  $U_{\text{pinning}}$  distribution contributing to the  $1/f^\gamma$  noise, as depicted in Fig. 3(a). For further fitting specifics, refer to Supplemental Material Note VIII [52] (Note VIII also contains Refs. [77, 94–96]).

To eliminate the background noise, we study the noise of discrete skyrmions at a constant field (Supplemental Material Note VI and Fig. S7 [52]). At a field where skyrmions are stabilized, multiple states with variable skyrmion numbers  $N_{\text{Skyr}}$  may be accessed through a field cycling process (Supplemental Material Note IV [52]). Figure 3(c) shows a linear variation of the relative Hall resistivity  $\Delta\rho_{xy}$  with  $N_{\text{Skyr}}$ . Each skyrmion contributes to  $\Delta\rho_{xy}$  in the amount of  $\Delta\rho_{xy}^{\text{Skyr}} = 17.6 \pm 1.25$  nΩ cm. This aligns closely with the previously reported electrical detection of an isolated skyrmion using the anomalous Hall effect [97]. In addition, the Hall resistance noise  $S_R$  also increases linearly with  $N_{\text{Skyr}}$  [Fig. 3(d)]. Fitting to  $S_R = S_{R,0} + \Delta S_R^{\text{Skyr}} N_{\text{Skyr}}$  yields the average contribution of each skyrmion to the noise  $\Delta S_R^{\text{Skyr}}$  as well as the contribution from the uniform magnetization state  $S_{R,0}$ . This fitting assumes negligible interactions between skyrmions due to their

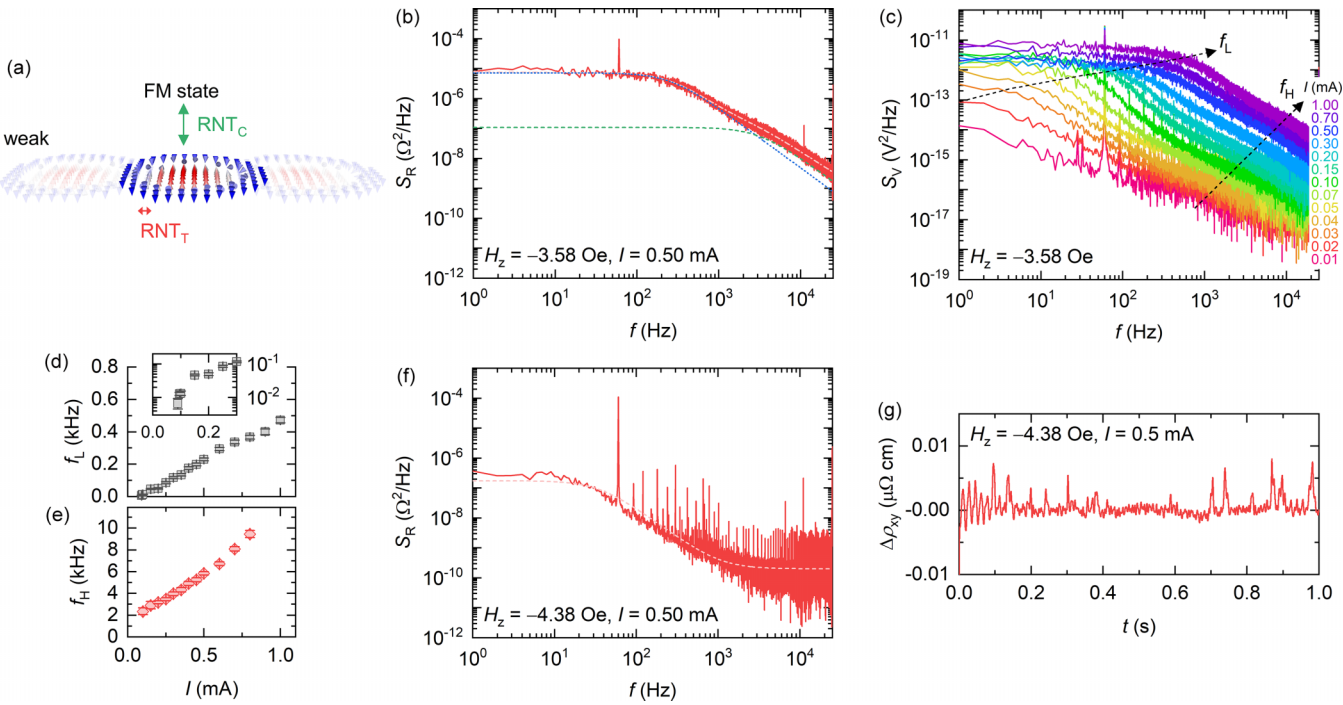


FIG. 5. Thermally induced and current-induced telegraphlike noise of a skyrmion in the weak pinning regime. (a) Schematic depiction of the skyrmion dynamics in the weak pinning regime. Skyrmions exhibit enhanced mobility as they readily hop between pinning sites. Both temperature and current can strongly affect the skyrmion dynamics. (b) Hall resistance noise  $S_R$  measured at  $H_z = -3.58$  Oe, where skyrmions are stabilized. The dash-dotted line is a fit to Eq. (3). The dotted blue and dashed green lines are fits to the lower- and higher-frequency telegraphlike noise, respectively. (c) Hall voltage noise  $S_V$  measured at various currents. The central frequency (d)  $f_L$  and (e)  $f_H$  of the lower- and higher-frequency telegraphlike noise as a function of current  $I$ . The inset in (d) presents a semilogarithmic plot to highlight the low current range. 1 mA current corresponds to the current density of  $1.2 \times 10^{10}$  A/m<sup>2</sup> flowing in the Ta buffer layer. (f) Hall resistance noise  $S_R$  measured at  $H_z = -4.38$  Oe. (g) Relative Hall resistivity  $\Delta\rho_{xy}$  variations in time at  $H_z = -4.38$  Oe, where only a single skyrmion may be nucleated. Nucleation of a skyrmion leads to an increase in  $\Delta\rho_{xy}$ , which reduces back to zero when the skyrmion propagates out of the Hall cross. All results are measured at 319.5 K.

large spatial separation (Supplemental Material Note VI [52]). Although  $\Delta S_R^{\text{Skyr}}$  is smaller than the background noise by one order of magnitude (Supplemental Material Fig. S7 [52]), it is distinguishable and clearly exhibits the  $1/f^\gamma$  signature [gray line in Fig. 3(b)]. Analogous measurements performed at different fields for this sample and other samples all concur with the  $1/f^\gamma$  signature with  $1.0 < \gamma < 1.4$ , independent of the polarization of the skyrmion (Supplemental Material Note VI and Fig. S8 [52]).

### B. Field-dependent $1/f^\gamma$ noise of a skyrmion

Figure 3(e) displays the field-dependent noise of a skyrmion at 10 Hz as well as the skyrmion diameter  $D_{\text{Skyr}}$ . It is noted that, while the skyrmion size decreases by  $\sim 43\%$  from  $-6.93$  to  $-9.24$  Oe [inset in Fig. 3(e)],  $\Delta S_R^{\text{Skyr}}$  decreases by almost two orders of magnitude. This is contrary to what one would expect, which is that the number of internal domain-wall hopping oscillators is proportional to the total length of domain walls which would thereby linearly affect the noise amplitude (Supplemental Material Note IX and Fig. S10 [52]). The significant reduction in noise with respect to the skyrmion size suggests that the number of internal domain-wall hopping oscillators in a skyrmion decreases significantly with a reduction in skyrmion size. It can be inferred that smaller skyrmions

are more appropriate for applications due to their substantially lower noise levels.

We calculate the signal-to-noise ratio (SNR) by using  $\sqrt{\Delta S_R^{\text{Skyr}}}/\Delta R_{xy}^{\text{Skyr}}$ , where  $\Delta R_{xy}^{\text{Skyr}}$  is the average contribution of each skyrmion to the anomalous Hall resistance. The SNR of a skyrmion is on the order of  $2.0\% \text{ Hz}^{-0.5}$  at 1 Hz and  $0.5\% \text{ Hz}^{-0.5}$  at 10 Hz, as evidenced by  $\text{SNR}^2 = \Delta S_R^{\text{Skyr}}/(\Delta R_{xy}^{\text{Skyr}})^2$  in Fig. 2(b). A low SNR is crucial in the electrical detection of a skyrmion owing to the small signal from this tiny magnetic structure [46,97].

### C. RTN of a skyrmion in the intermediate pinning regime

In the intermediate pinning regime, a skyrmion exhibits the ability to hop between certain pinning sites with greater ease yet remains strongly pinned by specific pinning centers (Supplemental Material Note X, Fig. S11, and Movie 4 [52]). The case presented here involves one part of a skyrmion being more strongly pinned while the other part, under thermal effects, fluctuates in time between two weaker pinning sites [Figs. 4(a) and 4(b)]. This behavior is schematically represented by the bended double-headed arrow in Fig. 4(a). This produces a RTN signature (Fig. 4(c), also see Ref. [45]). Along with the RTN, we identify a fluctuation in

$\Delta\rho_{xy}$  over time between two discrete states and correspondingly a skyrmion size variation between a small-skyrmion ( $\Delta\rho_{xy} \approx 0$ ) and a large-skyrmion ( $\Delta\rho_{xy} \approx 8 \text{ n}\Omega \text{ cm}$ ) configuration (Fig. 4(d) and Supplemental Material Movie 5 [52]). This shares the same physics as the internal domain-wall hopping oscillations in the strong pinning regime. There may also be more internal domain-wall hopping oscillations in the skyrmion, depicted by the straight double-headed arrow in Fig. 4(a). Nevertheless, these oscillations manifest with significantly smaller amplitudes  $\Delta V_H^2/2I^2$ . Their contributions to the overall noise [ $10^{-7}$  to  $10^{-6} \Omega^2/\text{Hz}$  at 1 Hz, as shown by the gray curve in Fig. 4(c)] are negligible in comparison with the detected noise in the intermediate pinning regime [ $10^{-5} \Omega^2/\text{Hz}$  at 1 Hz, as shown by the red curve in Fig. 4(c)].

The two identified states, referred to as the small- and large-skyrmion states, correspond to local minima in the energy landscape, separated by an energy barrier, as illustrated in Fig. 4(b). The fluctuation between these states is thermally induced, and the fluctuation rate is determined by the competition between the pinning energy barrier  $U_{\text{pinning}}$  and the thermal energy  $k_B T$ . Our previous work has shown that the energy landscape can be influenced by adjusting the applied magnetic field and a spin current through the Zeeman energy and spin-orbit torques, respectively [45]. This enables the manipulation of the local dynamics of a skyrmion and, in turn, influences the noise generated by the system [45]. The skyrmion is more likely being in the small-skyrmion state when the applied field  $H_z$  is increased or when the current is applied along the  $+x$  axis in Fig. 4(b) [45]. Similarly, the large-skyrmion state is more probable with decreasing the applied field or applying a current in the  $-x$  axis [45]. Along with the deterministic small- and large-skyrmion configurations at a higher or lower field, respectively, a  $1/f^\gamma$  noise signature is detected [Figs. 4(c) and 4(e)]. This closely resembles the behavior of a strongly pinned skyrmion.

#### D. Effects of the energy landscape on the internal domain-wall hopping oscillation dynamics

We observe and analyze the RTN for multiple isolated skyrmions where the fluctuation rate  $f_0$  varies between skyrmions (Fig. 4(f), also see Supplemental Material Note X and Fig. S12 [52]). This fluctuation rate variation is a result of different energy paths for the two-state transition and provides us with a platform to study how the energy landscape affects the internal domain-wall hopping oscillation dynamics of a skyrmion. The Arrhenius law  $f_0 = f_{00} \exp(-U_{\text{pinning}}/k_B T)$  tells us how  $U_{\text{pinning}}$  and the thermal energy  $k_B T$  affect the RTN dynamics. Additionally, the attempt frequency  $f_{00}$  may carry an activation entropy which implies that a longer path must be explored more randomly [98–100]. It has been identified recently through simulation studies that the entropic effect is crucial in describing other processes including the magnetization switching [98,100] and skyrmion annihilation [99]. The entropic effect can be elucidated through the forward flux sampling method, which involves a series of interfaces  $\{\lambda_0 = \lambda_L, \lambda_1, \dots, \lambda_{n-1}, \lambda_n = \lambda_S\}$  in configuration space between the large- and small-skyrmion states. These interfaces are defined as isosurfaces of a monotonically varying order parameter  $\zeta$ , such as the perpendicular magnetization

$m_z$  [Fig. 4(b)]. Despite the energy profile being characterized by two local minima and an energy barrier in between, re-crossings between neighboring interfaces are inevitable owing to the thermal energy. The fluctuation rate is then expressed as  $\prod_{i=0}^{n-1} P(\lambda_{i+1}|\lambda_i)$ , where  $P(\lambda_{i+1}|\lambda_i)$  represents the probability that a trajectory originating from  $\lambda_i$  reaching  $\lambda_{i+1}$  before returning to the basin initial state. For a large skyrmion size variation, more interfaces are required to transition from the basin large-skyrmion to the small-skyrmion state, reducing  $\prod_{i=0}^{n-1} P(\lambda_{i+1}|\lambda_i)$  and, consequently, the fluctuation rate. We illustrate in Fig. 4(e) that  $f_0$  increases when decreasing  $\Delta V_H^2/2I^2$ , with  $\Delta V_H^2/2I^2$  reflecting the skyrmion size variation. This provides evidence that, in addition to the  $U_{\text{pinning}}$  and thermal energy  $k_B T$ , the entropic effect is also crucial in the noise dynamics of a skyrmion.

We note that the RTN transitions into the  $1/f^\gamma$  noise by increasing  $N_{\text{Skyr}}$  (Supplemental Material Note X and Fig. S13 [52]). Each skyrmion represents a RTN oscillator. A collection of multiple skyrmions represents a system that verifies the  $1/f^\gamma$  signature arising from a collection of multiple internal domain-wall hopping oscillators.

#### E. Thermally induced and current-induced telegraphlike noise in the weak pinning regime

In the weak pinning regime, skyrmions exhibit enhanced mobility as they readily hop between pinning sites (Fig. 5(a), also see Supplemental Material Movie 2 and Fig. S3 [52]). In this scenario, we are unable to detect the electronic noise of a specified skyrmion. In addition to the thermal fluctuation, the current may also play a significant role in the dynamics.

In this section, we begin with displaying the  $S_R$  measured at  $H_z = -3.58 \text{ Oe}$ , where multiple skyrmions are stabilized (Supplemental Material Movie 6 [52]) to illustrate the noise signature and underlying physics [Figs. 5(b)–5(e)]. It is observed that skyrmions fit commensurably into the Hall cross at this field. However, this commensurability effect is not observed in the strong and intermediate pinning regimes, where the skyrmion order is constrained by the pinning sites.

We observe two telegraphlike noise signals in Fig. 5(b) which can be well fitted to

$$S_V = \frac{S_{V,0}^{\text{1Hz}}}{f^\gamma} + \frac{\Delta V_{H,L}^2/2f_L}{1 + (\pi f/f_L)^2} + \frac{\Delta V_{H,H}^2/2f_H}{1 + (\pi f/f_H)^2}, \quad (3)$$

where  $\Delta V_{H,L}^2/2I^2$  and  $\Delta V_{H,H}^2/2I^2$  are amplitudes of the lower- and higher-frequency telegraphlike signals, respectively. In our classification, we refer to this noise as telegraphlike noise instead of RTN because it arises from a collection of multiple internal domain-wall hopping RTN oscillators, though with a narrow distribution of these oscillators, as elaborated upon below. Notably, we confirm that the lower-frequency signal originates from the current effect as the central frequency  $f_L$  decreases and approaches zero when the current is decreased to zero [Figs. 5(c) and 5(d)]. The higher-frequency signal is dominated by the thermal effect since the central frequency  $f_H$  approaches a nonzero value ( $\sim 2 \text{ kHz}$ ) in the zero-current limit [Figs. 5(c) and 5(e)]. We note that the temperature induced by Joule heating, over the range of currents employed in this paper, remain  $< 1 \text{ K}$  (Supplemental Material Note XI

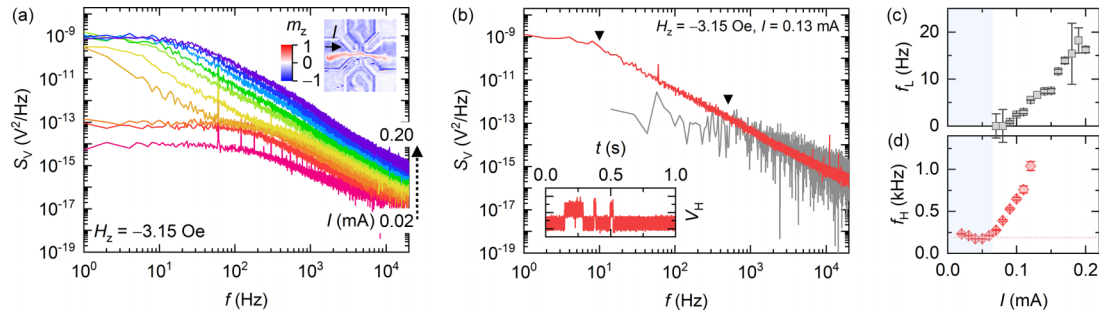


FIG. 6. Electronic noise of a bubble domain in a Hall cross with a dimension of  $5 \times 5 \mu\text{m}^2$ . (a) Hall voltage noise  $S_V$  measured at various currents. The inset shows a p-MOKE image of the Hall cross with a dimension of  $5 \times 5 \mu\text{m}^2$ , where only a single elongated magnetic bubble is nucleated and propagates through the Hall cross. (b)  $S_V$  measured at  $I = 0.13$  mA. The inset shows the Hall voltage variations in time at  $I = 0.13$  mA. The gray line is the power spectral density of the period between 0.15 and 0.22 s of Hall voltage signals. The central frequency (c)  $f_L$  and (d)  $f_H$  of the lower- and higher-frequency telegraphlike noise as a function of current  $I$ . All results are measured at 318.3 K. In this configuration, a current of 1 mA corresponds to a current density of  $4.8 \times 10^{10} \text{ A/m}^2$  flowing in the underlying Ta buffer layer.

and Fig. S14 [52]), which is negligible in comparison with the range of temperatures under our investigation.

When the magnetic field is increased to  $H_z = -4.38$  Oe, Hall resistance measurements in Fig. 5(g) show that only discrete skyrmions are nucleated and annihilated by the current, as evidenced by distinct spikes. As a result, the lower-frequency RTN is visible, while the higher-frequency signal dominated by thermal effects is suppressed. These observations suggest that the lower-frequency RTN arises from the current-induced skyrmion nucleation and annihilation process, which is discussed in further detail below.

We investigate the origins of the two noise signals by probing Hall voltage fluctuations over a smaller Hall cross with dimensions of  $5 \times 5 \mu\text{m}^2$ , where only a single magnetic bubble can be nucleated and propagate [inset in Fig. 6(a)]. We cannot ascertain whether the magnetic bubbles are topologically equivalent to skyrmions or not. To avoid any misleading, we refer to them as magnetic bubbles rather than skyrmions. However, this distinction does not impact our understanding of the origins of the two noise signals. We nucleate a magnetic bubble at defect positions or at sample boundaries. At a small current ( $\leq 0.06$  mA), the magnetic bubble domain is elongated and flows continuously through the Hall cross, and only the higher-frequency telegraphlike noise is visible [Fig. 6(a)]. By contrast, a larger current ( $\geq 0.07$  mA) induces discrete domain nucleation and propagation, causing the Hall voltage to fluctuate in time between two discrete states (inset in Fig. 6(b), also see Supplemental Material Movie 7 [52]). This thereby results in the additional lower-frequency bump [Figs. 6(a) and 6(b)]. The power spectrum over a period from 0.15 to 0.22 s of the Hall signal, again, only shows the higher-frequency signal [gray line in Fig. 6(b)]. During this time, a domain continuously flows through the Hall cross. These results indicate that the lower-frequency telegraph noise is a result of current-induced bubble domain nucleation and propagation, while the higher-frequency signal most likely arises from thermally dominated domain-wall fluctuations, as it is visible even with only a single bubble domain propagating through the Hall cross and has not been observed in the saturated ferromagnetic state. In the weak pinning regime,  $U_{\text{pinning}}$  exhibits a much narrower distribution. This

results in the telegraphlike noise signature [Figs. 5(b), 5(c), 6(a), and 6(b)], in contrast to  $1/f^\gamma$  noise signature in the strong pinning regime, with the measured frequency  $f_H$  being the averaged result over the domain-wall hopping oscillation dynamics.

#### IV. DISCUSSION AND CONCLUSIONS

In this paper, we have revealed comprehensive electronic noise properties of a single skyrmion. Distinctive amplitudes and frequency spectra can be mapped out according to the strong, intermediate, and weak pinning regimes. As summarized in Fig. 2, we detect a noise with a  $1/f^\gamma$  signature in the strong pinning regime but a RTN in the intermediate pinning regime and two telegraphlike signals in the weak pinning regime. Distinct noise signatures arise from the thermally dominated internal domain-wall hopping oscillation and/or the current-induced skyrmion nucleation. It is understood that the competition between the thermal and pinning energies governs the internal domain-wall hopping oscillation dynamics. Additionally, we reveal that the entropic effect is also significant in determining the dynamics and thereby the resulting noise signatures.

Our results demonstrate that noise fluctuation can serve as an insightful probe for characterizing the pinning condition of a skyrmion, with the  $1/f^\gamma$  signature indicating a flatter distribution of oscillators in the strong pinning regime [Fig. 3(a)]. In contrast, a much narrower distribution leads to telegraphlike noise in the weak pinning regime.

Furthermore, this paper has implications for applications that either require reliable electrical detection or utilize the inherent noise of a skyrmion. A comprehensive noise picture of a skyrmion can guide the fabrication of low-noise and reliable skyrmion-based devices. In the strong and intermediate pinning regimes, the skyrmion exhibits high thermal stability, but pinning effects impede its efficient manipulation. In contrast, a skyrmion can be efficiently manipulated in the weak pinning regime, although its thermal stability is reduced. We note that even a small current of  $6.1 \times 10^9 \text{ A/m}^2$  may cause the unwanted nucleation of a skyrmion [Figs. 5(f) and 5(g)], which may impose a current limit for applications.

Alternatively, artificial pinning centers may be used to guide a skyrmion along a desirable path and position it at a fixed location for detection. In this way, artificial pinning centers can help to achieve the tradeoff between energy efficiency and thermal stability necessary for applications. Noise fluctuation can also be an insightful probe for characterizing skyrmion interactions with artificial pinning.

Additionally, our noise study of a skyrmion may also be key to understanding the noise dynamics of other structures such as superconducting vortices [10] and charge density waves [23] that exhibit similar behaviors (Supplemental Material Note XII [52]). A complete picture connecting the noise

and the dynamics of these condensed matter states remains elusive and demands further exploration.

## ACKNOWLEDGMENTS

G.X. acknowledges funding support from the National Science Foundation (NSF) under Grant No. OMA-1936221. Y.Z. acknowledges funding support from the Fermilab-Graduate Instrumentation Research Award from U.S. Department of Energy Award No. DE-AC05-00OR22725. We use the Heidelberg MLA150 maskless aligner which is under the support of NSF Grant No. DMR-1827453.

---

[1] A. Van Der Ziel, On the noise spectra of semi-conductor noise and of flicker effect, *Physica* **16**, 359 (1950).

[2] M. Weissman,  $\frac{1}{f}$  noise and other slow, nonexponential kinetics in condensed matter, *Rev. Mod. Phys.* **60**, 537 (1988).

[3] P. Dutta and P. Horn, Low-frequency fluctuations in solids:  $\frac{1}{f}$  noise, *Rev. Mod. Phys.* **53**, 497 (1981).

[4] G. D'anna, P. Gammel, H. Safar, G. Alers, D. Bishop, J. Giapintzakis, and D. Ginsberg, Vortex-Motion-Induced Voltage Noise in  $\text{YBa}_2\text{Cu}_3\text{O}_{7-\delta}$  Single Crystals, *Phys. Rev. Lett.* **75**, 3521 (1995).

[5] Y. Togawa, R. Abiru, K. Iwaya, H. Kitano, and A. Maeda, Direct Observation of the Washboard Noise of a Driven Vortex Lattice in a High-Temperature Superconductor,  $\text{Bi}_2\text{Sr}_2\text{CaCu}_2\text{O}_y$ , *Phys. Rev. Lett.* **85**, 3716 (2000).

[6] S. A. Díaz, C. O. Reichhardt, D. P. Arovas, A. Saxena, and C. Reichhardt, Fluctuations and noise signatures of driven magnetic skyrmions, *Phys. Rev. B* **96**, 085106 (2017).

[7] T. Sato, W. Koshiba, A. Kikkawa, T. Yokouchi, H. Oike, Y. Taguchi, N. Nagaosa, Y. Tokura, and F. Kagawa, Slow steady flow of a skyrmion lattice in a confined geometry probed by narrow-band resistance noise, *Phys. Rev. B* **100**, 094410 (2019).

[8] T. Sato, A. Kikkawa, Y. Taguchi, Y. Tokura, and F. Kagawa, Mode locking phenomena of the current-induced skyrmion-lattice motion in microfabricated MnSi, *Phys. Rev. B* **102**, 180411(R) (2020).

[9] S. Okuma, J. Inoue, and N. Kokubo, Suppression of broadband noise at mode locking in driven vortex matter, *Phys. Rev. B* **76**, 172503 (2007).

[10] A. Marley, M. Higgins, and S. Bhattacharya, Flux Flow Noise and Dynamical Transitions in a Flux Line Lattice, *Phys. Rev. Lett.* **74**, 3029 (1995).

[11] C. Olson, C. Reichhardt, and F. Nori, Nonequilibrium Dynamic Phase Diagram for Vortex Lattices, *Phys. Rev. Lett.* **81**, 3757 (1998).

[12] T. Tsuboi, T. Hanaguri, and A. Maeda, Local Density Fluctuations of Moving Vortices in the Solid and Liquid Phases in  $\text{Bi}_2\text{Sr}_2\text{CaCu}_2\text{O}_y$ , *Phys. Rev. Lett.* **80**, 4550 (1998).

[13] J. M. Martinis, S. Nam, J. Aumentado, and C. Urbina, Rabi Oscillations in a Large Josephson-junction Qubit, *Phys. Rev. Lett.* **89**, 117901 (2002).

[14] E. Paladino, Y. Galperin, G. Falci, and B. Altshuler,  $\frac{1}{f}$  noise: Implications for solid-state quantum information, *Rev. Mod. Phys.* **86**, 361 (2014).

[15] O. S. Lumbroso, L. Simine, A. Nitzan, D. Segal, and O. Tal, Electronic noise due to temperature differences in atomic-scale junctions, *Nature (London)* **562**, 240 (2018).

[16] Y. Zhang and G. Xiao, Spin-dependent shot noise in  $\text{MgO}$ -based magnetic tunnel junctions under noncollinear magnetization alignment, *Phys. Rev. B* **100**, 224402 (2019).

[17] S. Larocque, E. Pinsolle, C. Lupien, and B. Reulet, Shot Noise of a Temperature-Biased Tunnel Junction, *Phys. Rev. Lett.* **125**, 106801 (2020).

[18] O. Shein-Lumbroso, J. Liu, A. Shastry, D. Segal, and O. Tal, Quantum Flicker Noise in Atomic and Molecular Junctions, *Phys. Rev. Lett.* **128**, 237701 (2022).

[19] R. Fleming and C. Grimes, Sliding-Mode Conductivity in  $\text{NbSe}_3$ : Observation of a Threshold Electric Field and Conduction Noise, *Phys. Rev. Lett.* **42**, 1423 (1979).

[20] G. Grüner, A. Zawadowski, and P. Chaikin, Nonlinear Conductivity and Noise Due to Charge-Density-Wave Depinning in  $\text{NbSe}_3$ , *Phys. Rev. Lett.* **46**, 511 (1981).

[21] I. Bloom, A. Marley, and M. Weissman, Nonequilibrium Dynamics of Discrete Fluctuators in Charge-Density Waves in  $\text{NbSe}_3$ , *Phys. Rev. Lett.* **71**, 4385 (1993).

[22] K. Bennaceur, C. Lupien, B. Reulet, G. Gervais, L. Pfeiffer, and K. West, Competing Charge Density Waves Probed by Nonlinear Transport and Noise in the Second and Third Landau Levels, *Phys. Rev. Lett.* **120**, 136801 (2018).

[23] M. Yoshida, T. Sato, F. Kagawa, and Y. Iwasa, Charge density wave dynamics in nonvolatile current-induced phase transition in  $1T\text{-TaS}_2$ , *Phys. Rev. B* **100**, 155125 (2019).

[24] A. K. Geremew, S. Rumenyantsev, B. Debnath, R. K. Lake, and A. A. Balandin, High-frequency current oscillations in charge-density-wave  $1T\text{-TaS}_2$  devices: Revisiting the “narrow band noise” concept, *Appl. Phys. Lett.* **116**, 163101 (2020).

[25] S. Mühlbauer, B. Binz, F. Jonietz, C. Pfleiderer, A. Rosch, A. Neubauer, R. Georgii, and P. Böni, Skyrmion lattice in a chiral magnet, *Science* **323**, 915 (2009).

[26] X. Yu, Y. Onose, N. Kanazawa, J. H. Park, J. Han, Y. Matsui, N. Nagaosa, and Y. Tokura, Real-space observation of a two-dimensional skyrmion crystal, *Nature (London)* **465**, 901 (2010).

[27] X. Yu, N. Kanazawa, Y. Onose, K. Kimoto, W. Zhang, S. Ishiwata, Y. Matsui, and Y. Tokura, Near room-temperature formation of a skyrmion crystal in thin-films of the helimagnet FeGe, *Nat. Mater.* **10**, 106 (2011).

[28] N. Romming, C. Hanneken, M. Menzel, J. E. Bickel, B. Wolter, K. von Bergmann, A. Kubetzka, and R. Wiesendanger, Writing and deleting single magnetic skyrmions, *Science* **341**, 636 (2013).

[29] W. Jiang, P. Upadhyaya, W. Zhang, G. Yu, M. B. Jungfleisch, F. Y. Fradin, J. E. Pearson, Y. Tserkovnyak, K. L. Wang, and O. Heinonen, Blowing magnetic skyrmion bubbles, *Science* **349**, 283 (2015).

[30] C. Moreau-Luchaire, C. Moutafis, N. Reyren, J. Sampaio, C. Vaz, N. Van Horne, K. Bouzehouane, K. Garcia, C. Deranlot, and P. Wernicke, Additive interfacial chiral interaction in multilayers for stabilization of small individual skyrmions at room temperature, *Nat. Nanotechnol.* **11**, 444 (2016).

[31] A. Soumyanarayanan, M. Raju, A. Gonzalez Oyarce, A. K. Tan, M.-Y. Im, A. P. Petrović, P. Ho, K. Khoo, M. Tran, and C. Gan, Tunable room-temperature magnetic skyrmions in Ir/Fe/Co/Pt multilayers, *Nat. Mater.* **16**, 898 (2017).

[32] K. Wang, V. Bheemarasetty, J. Duan, S. Zhou, and G. Xiao, Fundamental physics and applications of skyrmions: A review, *J. Magn. Magn. Mater.* **563**, 169905 (2022).

[33] I. Dzyaloshinsky, A thermodynamic theory of “weak” ferromagnetism of antiferromagnetics, *J. Phys. Chem. Solids* **4**, 241 (1958).

[34] T. Moriya, Anisotropic superexchange interaction and weak ferromagnetism, *Phys. Rev.* **120**, 91 (1960).

[35] A. Fert, V. Cros, and J. Sampaio, Skyrmions on the track, *Nat. Nanotechnol.* **8**, 152 (2013).

[36] K. Wang, L. Qian, S.-C. Ying, G. Xiao, and X. Wu, Controlled modification of skyrmion information in a three-terminal race-track memory, *Nanoscale* **11**, 6952 (2019).

[37] J. Tang, Y. Wu, W. Wang, L. Kong, B. Lv, W. Wei, J. Zang, M. Tian, and H. Du, Magnetic skyrmion bundles and their current-driven dynamics, *Nat. Nanotechnol.* **16**, 1086 (2021).

[38] W. Wang, D. Song, W. Wei, P. Nan, S. Zhang, B. Ge, M. Tian, J. Zang, and H. Du, Electrical manipulation of skyrmions in a chiral magnet, *Nat. Commun.* **13**, 1593 (2022).

[39] X. Zhang, M. Ezawa, and Y. Zhou, Magnetic skyrmion logic gates: Conversion, duplication and merging of skyrmions, *Sci. Rep.* **5**, 9400 (2015).

[40] Z. Yan, Y. Liu, Y. Guang, K. Yue, J. Feng, R. Lake, G. Yu, and X. Han, Skyrmion-based Programmable Logic Device with Complete Boolean Logic Functions, *Phys. Rev. Appl.* **15**, 064004 (2021).

[41] K. Raab, M. A. Brems, G. Beneke, T. Dohi, J. Rothörl, F. Kammerbauer, J. H. Mentink, and M. Kläui, Brownian reservoir computing realized using geometrically confined skyrmion dynamics, *Nat. Commun.* **13**, 6982 (2022).

[42] J. Zázvorka, F. Jakobs, D. Heinze, N. Keil, S. Kromin, S. Jaiswal, K. Litzius, G. Jakob, P. Virnau, and D. Pinna, Thermal skyrmion diffusion used in a reshuffler device, *Nat. Nanotechnol.* **14**, 658 (2019).

[43] Y. Jibiki, M. Goto, E. Tamura, J. Cho, S. Miki, R. Ishikawa, H. Nomura, T. Srivastava, W. Lim, and S. Auffret, Skyrmion Brownian circuit implemented in continuous ferromagnetic thin film, *Appl. Phys. Lett.* **117**, 082402 (2020).

[44] R. Ishikawa, M. Goto, H. Nomura, and Y. Suzuki, Implementation of skyrmion cellular automaton using Brownian motion and magnetic dipole interaction, *Appl. Phys. Lett.* **119**, 072402 (2021).

[45] K. Wang, Y. Zhang, V. Bheemarasetty, S. Zhou, S.-C. Ying, and G. Xiao, Single skyrmion true random number generator using local dynamics and interaction between skyrmions, *Nat. Commun.* **13**, 722 (2022).

[46] K. M. Song, J.-S. Jeong, B. Pan, X. Zhang, J. Xia, S. Cha, T.-E. Park, K. Kim, S. Finizio, and J. Raabe, Skyrmion-based artificial synapses for neuromorphic computing, *Nat. Electron.* **3**, 148 (2020).

[47] C. Reichhardt and C. O. Reichhardt, Noise fluctuations and drive dependence of the skyrmion Hall effect in disordered systems, *New J. Phys.* **18**, 095005 (2016).

[48] R. Gruber, J. Zázvorka, M. A. Brems, D. R. Rodrigues, T. Dohi, N. Kerber, B. Seng, M. Vafaei, K. Everschor-Sitte, and P. Virnau, Skyrmion pinning energetics in thin film systems, *Nat. Commun.* **13**, 3144 (2022).

[49] K. Litzius, J. Leliaert, P. Bassirian, D. Rodrigues, S. Kromin, I. Lemesh, J. Zázvorka, K.-J. Lee, J. Mulders, and N. Kerber, The role of temperature and drive current in skyrmion dynamics, *Nat. Electron.* **3**, 30 (2020).

[50] X. Zhang, N. Vernier, W. Zhao, H. Yu, L. Vila, Y. Zhang, and D. Ravelosona, Direct Observation of Domain-Wall Surface Tension by Deflating or Inflating a Magnetic Bubble, *Phys. Rev. Appl.* **9**, 024032 (2018).

[51] S. Lemerle, J. Ferré, C. Chappert, V. Mathet, T. Giamarchi, and P. Le Doussal, Domain Wall Creep in an Ising Ultrathin Magnetic Film, *Phys. Rev. Lett.* **80**, 849 (1998).

[52] See Supplemental Material at <http://link.aps.org/supplemental/10.1103/PhysRevB.108.094431> for details on sample fabrication (Note I), experimental setup (Note II), magnetic properties of the magnetic multilayer (Note III), evidence of skyrmions and their manipulations (Note IV), effects of the sputtering rate on the pinning of magnetic structures (Note V), micromagnetic simulations of skyrmion noise (Note VI), estimate of the strength of pinning (Note VII), noise of domain walls (Note VIII), and additional experimental results and discussions (Notes IX - XII).

[53] H. Yang, M. Chshiev, B. Dieny, J. Lee, A. Manchon, and K. Shin, First-principles investigation of the very large perpendicular magnetic anisotropy at Fe|MgO and Co|MgO interfaces, *Phys. Rev. B* **84**, 054401 (2011).

[54] B. Dieny and M. Chshiev, Perpendicular magnetic anisotropy at transition metal/oxide interfaces and applications, *Rev. Mod. Phys.* **89**, 025008 (2017).

[55] G. Yu, P. Upadhyaya, Y. Fan, J. G. Alzate, W. Jiang, K. L. Wong, S. Takei, S. A. Bender, L.-T. Chang, and Y. Jiang, Switching of perpendicular magnetization by spin-orbit torques in the absence of external magnetic fields, *Nat. Nanotechnol.* **9**, 548 (2014).

[56] B. Rodmacq, A. Manchon, C. Ducruet, S. Auffret, and B. Dieny, Influence of thermal annealing on the perpendicular magnetic anisotropy of Pt/Co/AlOx trilayers, *Phys. Rev. B* **79**, 024423 (2009).

[57] M. Xu, M. Li, P. Khanal, A. Habiboglu, B. Insana, Y. Xiong, T. Peterson, J. C. Myers, D. Ortega, and H. Qu, Voltage-controlled Antiferromagnetism in Magnetic Tunnel Junctions, *Phys. Rev. Lett.* **124**, 187701 (2020).

[58] Y. Fan, K. Smith, G. Lüpke, A. Hanbicki, R. Goswami, C. Li, H. Zhao, and B. Jonker, Exchange bias of the interface spin system at the Fe/MgO interface, *Nat. Nanotechnol.* **8**, 438 (2013).

[59] L. Qian, K. Wang, Y. Zheng, and G. Xiao, Spin Hall effect in the  $\alpha$  and  $\beta$  phases of  $Ta_xW_{1-x}$  alloys, *Phys. Rev. B* **102**, 094438 (2020).

[60] R. L. Conte, E. Martinez, A. Hrabec, A. Lamperti, T. Schulz, L. Nasi, L. Lazzarini, R. Mantovan, F. Maccherozzi, and S. Dhesi, Role of B diffusion in the interfacial Dzyaloshinskii-Moriya interaction in  $Ta/Co_{20}Fe_{60}B_{20}/MgO$  nanowires, *Phys. Rev. B* **91**, 014433 (2015).

[61] M. Cecot, Ł. Karwacki, W. Skowroński, J. Kanak, J. Wrona, A. Żywczak, L. Yao, S. van Dijken, J. Barnaś, and T. Stobiecki, Influence of intermixing at the  $Ta/CoFeB$  interface on spin Hall angle in  $Ta/CoFeB/MgO$  heterostructures, *Sci. Rep.* **7**, 968 (2017).

[62] J. J. Senkevich, T. Karabacak, D.-L. Bae, and T. S. Cale, Formation of body-centered-cubic tantalum via sputtering on low- $\kappa$  dielectrics at low temperatures, *J. Vac. Sci. Technol.* **24**, 534 (2006).

[63] H. Zhang, S. Yamamoto, Y. Fukaya, M. Maekawa, H. Li, A. Kawasuso, T. Seki, E. Saitoh, and K. Takanashi, Current-induced spin polarization on metal surfaces probed by spin-polarized positron beam, *Sci. Rep.* **4**, 4844 (2014).

[64] J. J. Colin, G. Abadias, A. Michel, and C. Jaouen, On the origin of the metastable  $\beta$ -Ta phase stabilization in tantalum sputtered thin films, *Acta Mater.* **126**, 481 (2017).

[65] E. A. Ellis, M. Chmielus, and S. P. Baker, Effect of sputter pressure on Ta thin films: Beta phase formation, texture, and stresses, *Acta Mater.* **150**, 317 (2018).

[66] S. Sato, T. Inoue, and H. Sasaki, Thermal oxidation of  $\beta$ -Ta below 500 °C, *Thin. Solid. Films* **86**, 21 (1981).

[67] Q. Hao, W. Chen, and G. Xiao, Beta ( $\beta$ ) tungsten thin films: Structure, electron transport, and giant spin Hall effect, *Appl. Phys. Lett.* **106**, 182403 (2015).

[68] A. Patterson, The Scherrer formula for x-ray particle size determination, *Phys. Rev.* **56**, 978 (1939).

[69] E. Zubler, The gettering properties of tantalum, *J. Electrochem. Soc.* **110**, 1072 (1963).

[70] Y. A. Vodakov, A. Roenkov, M. Ramm, E. Mokhov, and Y. N. Makarov, Use of Ta-container for sublimation growth and doping of SiC bulk crystals and epitaxial layers, *Phys. Status Solidi B* **202**, 177 (1997).

[71] T. F. K. Lilov, S. O. S. Ohshima, and S. N. S. Nishino, Effect of tantalum in crystal growth of silicon carbide by sublimation close space technique, *Jpn. J. Appl. Phys.* **40**, 6737 (2001).

[72] E. Krikorian and R. Sneed, Deposition of tantalum, tantalum oxide, and tantalum nitride with controlled electrical characteristics, *J. Appl. Phys.* **37**, 3674 (1966).

[73] L. Feinstein and R. Hüttemann, Factors controlling the structure of sputtered Ta films, *Thin. Solid. Films* **16**, 129 (1973).

[74] R. Knepper, B. Stevens, and S. P. Baker, Effect of oxygen on the thermomechanical behavior of tantalum thin films during the  $\beta$ - $\alpha$  phase transformation, *J. Appl. Phys.* **100**, 123508 (2006).

[75] T. Meier, M. Kronseder, and C. Back, Domain-width model for perpendicularly magnetized systems with Dzyaloshinskii-Moriya interaction, *Phys. Rev. B* **96**, 144408 (2017).

[76] I. Lemeshev, F. Büttner, and G. S. Beach, Accurate model of the stripe domain phase of perpendicularly magnetized multilayers, *Phys. Rev. B* **95**, 174423 (2017).

[77] A. B. Kolton, A. Rosso, T. Giamarchi, and W. Krauth, Creep dynamics of elastic manifolds via exact transition pathways, *Phys. Rev. B* **79**, 184207 (2009).

[78] V. Jeudy, A. Mougin, S. Bustingorry, W. S. Torres, J. Gorchon, A. B. Kolton, A. Lemaître, and J.-P. Jamet, Universal Pinning Energy Barrier for Driven Domain Walls in Thin Ferromagnetic Films, *Phys. Rev. Lett.* **117**, 057201 (2016).

[79] K. Shahbazi, J.-V. Kim, H. T. Nembach, J. M. Shaw, A. Bischof, M. D. Rossell, V. Jeudy, T. A. Moore, and C. H. Marrows, Domain-wall motion and interfacial Dzyaloshinskii-Moriya interactions in  $Pt/Co/Ir(t_{lr})/Ta$  multilayers, *Phys. Rev. B* **99**, 094409 (2019).

[80] W. S. Torres, R. D. Pardo, S. Bustingorry, A. B. Kolton, A. Lemaître, and V. Jeudy, Universal dimensional crossover of domain wall dynamics in ferromagnetic films, *Phys. Rev. B* **99**, 201201(R) (2019).

[81] M. Sampietro, L. Fasoli, and G. Ferrari, Spectrum analyzer with noise reduction by cross-correlation technique on two channels, *Rev. Sci. Instrum.* **70**, 2520 (1999).

[82] K. Wang, Y. Zhang, and G. Xiao, Anomalous Hall Sensors with High Sensitivity and Stability Based on Interlayer Exchange-Coupled Magnetic Thin Films, *Phys. Rev. Appl.* **13**, 064009 (2020).

[83] Y. Zhang, K. Wang, and G. Xiao, Noise characterization of ultrasensitive anomalous Hall effect sensors based on  $Co_{40}Fe_{40}B_{20}$  thin films with compensated in-plane and perpendicular magnetic anisotropies, *Appl. Phys. Lett.* **116**, 212404 (2020).

[84] K. Wang, Y. Zhang, S. Zhou, and G. Xiao, Micron-scale anomalous Hall sensors based on  $Fe_xPt_{1-x}$  thin films with a large Hall angle and near the spin-reorientation transition, *Nanomaterials* **11**, 854 (2021).

[85] N. Nagaosa, J. Sinova, S. Onoda, A. H. MacDonald, and N. P. Ong, Anomalous Hall effect, *Rev. Mod. Phys.* **82**, 1539 (2010).

[86] L. Liu, C.-F. Pai, Y. Li, H. Tseng, D. Ralph, and R. Buhrman, Spin-torque switching with the giant spin Hall effect of tantalum, *Science* **336**, 555 (2012).

[87] Q. Hao and G. Xiao, Giant spin Hall effect and magnetotransport in a  $Ta/CoFeB/MgO$  layered structure: A temperature dependence study, *Phys. Rev. B* **91**, 224413 (2015).

[88] K. Wang, L. Qian, W. Chen, S.-C. Ying, G. Xiao, and X. Wu, Spin torque effect on topological defects and transitions of magnetic domain phases in  $Ta/CoFeB/MgO$ , *Phys. Rev. B* **99**, 184410 (2019).

[89] X. Wang, H. Yuan, and X. Wang, A theory on skyrmion size, *Commun. Phys.* **1**, 31 (2018).

[90] S.-Z. Lin, C. Reichhardt, C. D. Batista, and A. Saxena, Particle model for skyrmions in metallic chiral magnets: Dynamics, pinning, and creep, *Phys. Rev. B* **87**, 214419 (2013).

[91] O. I. Utesov, Thermodynamically stable skyrmion lattice in a tetragonal frustrated antiferromagnet with dipolar interaction, *Phys. Rev. B* **103**, 064414 (2021).

[92] C. Song, N. Kerber, J. Rothörl, Y. Ge, K. Raab, B. Seng, M. A. Brems, F. Dittrich, R. M. Reeve, and J. Wang, Commensurability between element symmetry and the number of skyrmions governing skyrmion diffusion in confined geometries, *Adv. Funct. Mater.* **31**, 2010739 (2021).

[93] A. Vansteenkiste, J. Leliaert, M. Dvornik, M. Helsen, F. Garcia-Sanchez, and B. Van Waeyenberge, The design and verification of MuMax3, *AIP Advances* **4**, 107133 (2014).

[94] A. Gurevich, Distribution of pinning energies and the resistive transition in superconducting films, *Phys. Rev. B* **42**, 4857 (1990).

[95] S. Demirdi $\ddot{s}$ , C. J. van der Beek, Y. Fasano, N. R. Cejas Bolecek, H. Pastoriza, D. Colson, and F. Rullier-Albenque, Strong pinning and vortex energy distributions in single-crystalline  $\text{Ba}(\text{Fe}_{1-x}\text{Co}_x)_2\text{As}_2$ , *Phys. Rev. B* **84**, 094517 (2011).

[96] V. Sandu, A. M. Ionescu, G. Aldica, M. A. Grigoroscuta, M. Burdusel, and P. Badica, On the pinning force in high density  $\text{MgB}_2$  samples, *Sci. Rep.* **11**, 5951 (2021).

[97] D. Maccariello, W. Legrand, N. Reyren, K. Garcia, K. Bouzehouane, S. Collin, V. Cros, and A. Fert, Electrical detection of single magnetic skyrmions in metallic multilayers at room temperature, *Nat. Nanotechnol.* **13**, 233 (2018).

[98] L. Desplat and J.-V. Kim, Entropy-Reduced Retention Times in Magnetic Memory Elements: A Case of the Meyer-Neldel Compensation Rule, *Phys. Rev. Lett.* **125**, 107201 (2020).

[99] L. Desplat, C. Vogler, J.-V. Kim, R. L. Stamps, and D. Suess, Path sampling for lifetimes of metastable magnetic skyrmions and direct comparison with Kramers' method, *Phys. Rev. B* **101**, 060403(R) (2020).

[100] L. Desplat and J.-V. Kim, Quantifying the Thermal Stability in Perpendicularly Magnetized Ferromagnetic Nanodisks with Forward Flux Sampling, *Phys. Rev. Appl.* **14**, 064064 (2020).